



Article

# Study of the Structural, Electrical, and Mechanical Properties and Morphological Features of Y-Doped CeO<sub>2</sub> Ceramics with Porous Structure

Rafael I. Shakirzyanov <sup>1</sup>, Natalia O. Volodina <sup>1</sup>, Artem L. Kozlovskiy <sup>1,2,\*</sup>, Maxim V. Zdorovets <sup>1,2</sup>, Dmitriy I. Shlimas <sup>1,2</sup>, Daryn B. Borgekov <sup>1,2</sup> and Yuriy A. Garanin <sup>1</sup>

<sup>1</sup> Engineering Profile Laboratory, L.N. Gumilyov Eurasian National University, Satpayev St., Astana 010008, Kazakhstan; jorge.r2448@gmail.com

<sup>2</sup> Laboratory of Solid State Physics, The Institute of Nuclear Physics, Almaty 050032, Kazakhstan

\* Correspondence: kozlovskiy.a@inp.kz; Tel./Fax: +77-024-4133-68

**Abstract:** In this work, ceramic samples of cerium oxide doped with yttrium were investigated. The concentration of a dopant Y(NO<sub>3</sub>)<sub>3</sub> varied from 5 to 25 wt% in the initial charge. In the course of the experiment, a simple method was developed to obtain ceramics with a porosity of ~20% via one-step annealing in air in a muffle furnace. For comparison, samples with two annealings were also synthesized to determine the effects of pores on electrical, structural, and mechanical characteristics. The obtained samples were examined via X-ray powder diffraction, scanning electron microscopy, X-ray energy dispersive spectroscopy, Raman spectroscopy, dielectric spectroscopy, and Vickers microhardness measurements. The substitution of Ce<sup>4+</sup> ions with Y<sup>3+</sup> ions led to a significant decrease in the lattice parameter, average crystallite size, and average grain size, with a simultaneous increase in the lattice defectivity, dielectric constant, electrical conductivity, and microhardness values. It is shown that samples with a dopant weight fraction of 0.05–0.15 and one-step annealing have favorable electrical and mechanical characteristics for energy applications as porous materials with ionic conductivity.

**Keywords:** ceria ceramics; permittivity; microhardness; porous ceramics; solid-state sintering



**Citation:** Shakirzyanov, R.I.; Volodina, N.O.; Kozlovskiy, A.L.; Zdorovets, M.V.; Shlimas, D.I.; Borgekov, D.B.; Garanin, Y.A. Study of the Structural, Electrical, and Mechanical Properties and Morphological Features of Y-Doped CeO<sub>2</sub> Ceramics with Porous Structure. *J. Compos. Sci.* **2023**, *7*, 411. <https://doi.org/10.3390/jcs7100411>

Academic Editor: Francesco Tornabene

Received: 26 August 2023

Revised: 6 September 2023

Accepted: 28 September 2023

Published: 4 October 2023



**Copyright:** © 2023 by the authors. Licensee MDPI, Basel, Switzerland. This article is an open access article distributed under the terms and conditions of the Creative Commons Attribution (CC BY) license (<https://creativecommons.org/licenses/by/4.0/>).

## 1. Introduction

Currently, scientists worldwide are looking for new materials that can fulfill the increasing requirements of the power industry. Ceramics made from metal oxides and nitrides have favorable functional and structural properties, leading to their extensive use in the field of power engineering [1]. Specific examples of applications include ceramics employed as inert matrices for dispersed nuclear fuel [2,3], ceramics designed for solid oxide fuel cells [4], ceramics utilized in the generation of hydrogen through two-stage thermochemical water separation cycles [5], and ceramic additives incorporated into polymer membrane electrolytes [6].

Cerium oxide (CeO<sub>2</sub>), also known as ceria, is a multifunctional material suitable for these applications. CeO<sub>2</sub> exhibits exceptional heat resistance due to its high melting point of approximately 2750 K. Fluorite-type crystal lattice (space group Fm3m) allows CeO<sub>2</sub> to withstand irradiation by energetic particles without undergoing amorphization. As a result, the material demonstrates remarkable stability against radiation effects. Cerium oxide is characterized by a density ranging from 6.44 to 6.76 g/cm<sup>3</sup>, thermal conductivity of 2–6 W/m·K, and specific heat capacity in the range of 0.35 to 0.45 J/g·K within a temperature interval of 273 to 1473 K [7]. The coefficient of thermal expansion of CeO<sub>2</sub> is 10–12.5 × 10<sup>-6</sup> K<sup>-1</sup>. Moreover, it demonstrates Young's modulus values ranging from 207 to 228 GPa, shear modulus values of 79 to 86 GPa, and bulk modulus values ranging from 185 to 208 GPa [8].

These parameters are very important for the manufacture of structural materials for nuclear power engineering. One of the most promising applications of ceramic materials in this field is the creation of inert matrices of dispersed nuclear fuel. Within these matrices, the nuclear fuel (e.g., plutonium oxide) is uniformly distributed throughout the volume of the fuel cell. In particular, the dispersed fuel matrix material has the following requirements: good thermal conductivity; insolubility in hot water; high melting point (~3000 K); chemical inertness; compatibility with nuclear reactor materials; and transparency to thermal neutrons. Cerium oxide is an excellent candidate for the role of an inert matrix in dispersed nuclear fuels. The inert matrix/nuclear fuel composite will have more advantageous structural properties compared to conventional structural materials. This would increase fuel production in solid fuel cells and improve the efficiency of the nuclear reactor [9]. In addition, the use of dispersed fuel opens up the possibility of using safer nuclear fuel and creating a reprocessing cycle for military weapons-grade plutonium [10].

In the case of solid oxide fuel cells, materials are required to have high ionic conductivity, chemical resistance under redox reaction conditions, relatively high electronic conductivity, and mechanical strength. These properties can be realized in doped ceramics with cerium. When substituting cerium with elements of lower valence, it is possible to create oxygen vacancies, which, in turn, can significantly change the ionic conductivity of ceramics. Relatively high electronic conductivity is possible due to the hopping mechanism caused by the existence of  $\text{Ce}^{3+}$  and  $\text{Ce}^{4+}$  cations. For doped  $\text{CeO}_2$ , the operating temperatures as a solid oxide fuel cell are in the range of 773–973 K. In this temperature range, the current flow follows the mechanism of ionic conductivity.

Doping  $\text{CeO}_2$  with Y, Sm, or Gd shows improved properties due to enhanced ionic conductivity [11,12]. Substitution of Ce ions with Sm, Ca, Y, Gd, and La ions leads to high conductivity values at 873 K of  $1.13 \times 10^{-3}$  to  $7.7 \times 10^{-2}$  S/cm [4]. Impedance spectra of the obtained doped ceramics show that at temperatures above 573 K, Ca-doped cerium oxide samples have improved ionic conductivity, with charge transfer occurring mainly through the grains (grain conductivity) [13]. The introduction of calcium cations changes the charge state of cerium oxide, in which anionic vacancies are formed. The presence of such vacancies can improve the ionic conductivity of cerium ceramics.

These changes are especially intriguing when tetravalent cerium ions in the fluorite lattice are replaced by a trivalent dopant ion. As a result, oxygen vacancies are created in the anionic sublattice in order to balance the charge [14,15]. The geometry, structure, and properties of these defects resulting from atomic substitution depend not only on the nature of the dopant (e.g., its crystal structure, electronic charge, ionic radius, electronegativity, etc.) but also on the mole fraction in the host matrix [16].

In previous works, much effort has been invested in the study of substitution with different ions on the electrical and mechanical properties and morphological features of ceria ceramics [4,13,17]. These studies showed the effectiveness of this approach in improving the performance of the solid fuel cell element. Another known approach to modifying the properties of solid fuel cell elements, ceria-based electrolytes, and hydrogen generation systems is the creation of porous ceramic structures [18,19]. This study aimed to assess the effect of variations in the dopant concentration on the electrical, mechanical, phase, and morphological characteristics of cerium oxide ceramics. In addition, highly porous ceria ceramics with the same composition were also synthesized to investigate the effects of pore formation during the sintering process on the physical and structural properties. To achieve this goal, a simple method, including yttrium nitrate usage as the initial precursor for pore formation, was implemented. The research involved the synthesis of  $\text{CeO}_2$  ceramics doped with Y, followed by a comprehensive analysis employing techniques such as X-ray powder diffraction (XRD), Raman spectroscopy, scanning electron microscopy, dielectric spectroscopy, and Vickers microhardness testing. XRD and Raman spectroscopy are very useful tools for confirming the successful substitution of  $\text{Ce}^{4+}$  ions when dielectric spectroscopy can show changes in electric properties in doped ceria ceramics. This is very important for the evaluation of the applicability of synthesized experimental sam-

ples as solid oxide electrolytes. Vickers microhardness can show variations in mechanical characteristics, which can help with finding the optimal porosity for practical applications.

## 2. Experimental Section

Ceramic samples for the study were obtained via the conventional solid-state method, including the mixing of initial components into a homogeneous mixture, compaction, and sintering. Two series of samples were prepared: in the first series, one annealing of the initial charge after compacting was performed; in the second series, two annealings were conducted. For the first series of samples (one annealing), the fabrication route included the following operations: weighing → mixing, homogenization → plasticizer addition → compaction → final annealing. The second series of samples (two annealings) was fabricated according to the following route: weighing → mixing, homogenization → pre annealing for nitrate combustion → milling → plasticizer addition → compacting → final annealing.

Cerium oxide  $\text{CeO}_2$  and yttrium nitrate  $\text{Y}(\text{NO}_3)_3$  (Sigma Aldrich, high purity, St. Louis, MO, USA) in the form of powders less than  $5 \mu\text{m}$  in size were used as starting reagents. The mixture was weighed according to the formula  $(1 - x) \cdot \text{CeO}_2 + x \cdot \text{Y}(\text{NO}_3)_3$ , where  $x$  is the weight concentration. A Fritsch Pulverisette 6 planetary mill was used for homogenization of the mixture (and milling) of the powders. Dry milling was performed in grinding bowls with tungsten carbide balls for 30 min at a speed of 250 rpm. Milling after pre-annealing for nitrate decomposition was conducted for 1 h. An aqueous solution of polyvinyl alcohol (10 wt%) was used as a plasticizer. Compacting was performed on a hydraulic press in a stainless steel mold. The green pellets for subsequent annealing were in the form of tablets with an outer diameter of 12.1 mm and a thickness of 1.2 mm. Air annealing was performed in a muffle furnace with resistive heaters. Pre-annealing for the decomposition of nitrate from the charge was performed at  $900 \text{ }^\circ\text{C}$  for 2 h, and the annealing of the pellets was performed for 5 h at  $1500 \text{ }^\circ\text{C}$  (heating rate  $10 \text{ }^\circ\text{C}/\text{min}$ ).

The apparent density measurements of both series of sintered tablets were conducted using a micrometer and high-precision scales. Powder diffraction patterns were registered in Bragg–Brentano geometry on a Bruker D8 Advance diffractometer (Bruker GmbH, Mannheim, Germany). The conditions for recording the diffraction pattern were as follows:  $\text{CuK}\alpha$  radiation (wavelength  $\lambda = 1.5406 \text{ \AA}$ ); scanning rate of  $1.8^\circ/\text{min}$ ; angular range of  $2\theta = 20\text{--}75^\circ$ . The Profex 5.2.0 program [20] was utilized for processing the diffraction patterns using the Rietveld refinement method. Scanning electron microscopy (SEM) microphotographs and energy-dispersive X-ray spectroscopy (elemental composition) spectra were obtained using a Phenom ProX G6 microscope (Thermo Fisher Scientific, Eindhoven, The Netherlands). The chemical composition was averaged from measurements taken at five points across different areas of the sample. The samples were also investigated via Raman spectroscopy on an EnSpectr M532 spectrometer (Spectr-M LLC, Chernogolovka, Russia) at a laser wavelength of 532 nm.

Frequency spectra of the dielectric permittivity ( $\epsilon'$ ) and the tangent of the dielectric loss angle ( $\tan \delta$ ) were measured using an RLC meter model HIOKI IM3533-01 (manufactured by Hioki E.E Corporation, Singapore) at room temperature. Prior to conducting measurements, a conductive silver paste was applied to the surfaces of the tablets to create a flat capacitor configuration. The samples were subsequently dried in an oven at  $60 \text{ }^\circ\text{C}$  for a duration of 24 h. The conversion of measured data to dielectric permittivity was calculated utilizing the formula  $\epsilon' = \frac{C}{\epsilon_0 S}$ , where  $h$  denotes the thickness of the tablet,  $S$  represents the electrode surface area,  $C$  signifies the capacitance, and  $\epsilon_0$  is the dielectric constant. The calculation of alternating current conductivity ( $\sigma_{AC}$ ) was derived using the formula  $\sigma_{AC} = 2\pi f \epsilon_0 \epsilon' \tan \delta$ , where  $f$  corresponds to the frequency of the measurement. The Vickers microhardness was measured using a MIKON Duroline-M1 microhardness tester (manufactured by METKON instruments, Bursa, Turkey) with an applied load of 0.2 kgf. Additionally, optical microscopy micrographs of the surface of the samples were acquired via an optical microhardness tester system.

### 3. Results and Discussion

The results of the phase analysis of the synthesized ceramics with concentrations ranging from  $x = 0.00$  to  $0.25$  indicate that the investigated samples have a cubic phase with the Fm-3m space group (fluorite structure). Identical diffraction patterns were obtained for samples subjected to one and two annealings. Experimental and calculated diffraction patterns using the Rietveld refinement method are presented in Figure 1. The Rietveld refinement method was employed to calculate the parameters of the crystalline structure. The calculated values with their corresponding statistical convergence parameters are listed in Table 1. The obtained convergence parameters signify a favorable agreement between the model and experiment. As evident from Table 1, an increase in dopant concentration leads to a decrease in the lattice parameter, which is attributed to the formation of oxygen vacancies [21,22]. It is worth noting that the formation of oxygen vacancies is primarily driven by the crystal's tendency to neutralize the charge imbalance resulting from the substitution of  $\text{Ce}^{4+}$  ions with  $\text{Y}^{3+}$  ions of lower oxidation states. Ceramics composed of cerium oxide doped with yttrium can be described via the chemical formula  $\text{Ce}_{1-y}\text{Y}_y\text{O}_{2-y/2}$ . In this formula, it is evident that the substitution of cerium ions by yttrium ions leads to a reduction in the number of oxygen cations within the formula unit. If the substitution does not result in the formation of new phases, oxygen vacancies are created to compensate for the excessive negative charge within the crystal lattice.

**Table 1.** Dependence of lattice parameters  $a$  and X-ray density on dopant concentration.

X	$a$ , Å	X-ray Density, g/cm <sup>3</sup>	R <sub>exp</sub>	R <sub>wp</sub>	GOF	$\chi^2$
0.00	5.411094 ± 0.000052	7.215	6.63	9.47	1.43	2.04
0.05	5.410745 ± 0.000030	7.182	6.55	7.26	1.11	1.23
0.10	5.410057 ± 0.000037	7.115	6.50	7.05	1.08	1.18
0.15	5.408659 ± 0.000074	7.015	6.46	8.89	1.38	1.89
0.20	5.408249 ± 0.000045	6.877	5.86	6.61	1.13	1.27
0.25	5.406372 ± 0.000067	6.841	6.24	7.35	1.19	1.41

During the refinement using the Rietveld method, in order to enhance convergence parameters, yttrium ions were introduced into the initial  $\text{CeO}_2$  lattice at the atomic position of the Ce ion (Wyckoff  $a$ ,  $x = 0.00$ ,  $y = 0.00$ ,  $z = 0.00$ ). The quantity of yttrium ions was adjusted to minimize the standard deviation  $\chi^2$ . In general, the yttrium content per formula unit deviated by  $\pm 0.03$  from the calculated mass concentrations  $x$ , indicating the possible loss of a certain amount of yttrium during nitrate decomposition or segregation of yttrium atoms at grain boundaries. The latter phenomenon has been observed, for instance, in ceramics with a fluorite-type zirconium oxide structure stabilized with yttrium [23]. The calculated X-ray density, as well as the lattice parameter  $a$ , also decreases with an increase in dopant concentration  $x$ .

The diffraction peaks (111), (200), (220), (311), (222), and (400) were fitted using the pseudo-Voigt function to extract parameters such as the peak center on the  $2\theta$  axis and the full width at half maximum ( $B_t$ ). This approximation was employed for microstrain calculations following the Williamson–Hall method [24]. Additionally, the average sizes of the crystallites ( $d_{av}$ ) were determined using the Debye–Scherrer formula. The calculated results, depicted as dependencies of  $B_t \cos(\theta)(4\sin(\theta))$ , are presented in both Figure 2 and Table 2. From the calculated microstrain values (Table 2), it can be seen that compressive stresses exist within the fluorite lattice of both the original  $\text{CeO}_2$  ceramic and the yttrium-doped. However, an increase in the dopant concentration results in a reduction in the stress modulus, a trend that contradicts prior investigations of  $\text{CeO}_2$  oxides [25,26]. These investigations have revealed that in studies where the crystallite size ( $d_{av}$ ) increases, there is a decrease in the microstrain within the lattice. However, the present study presents an opposite trend, as observed in Table 2. The potential reasons for this discrepancy will be discussed further in the text. Additionally, it is worth noting that an increase in the dopant concentration leads to an

increase in dislocation density, calculated based on the average crystallite size ( $d_{av}$ ) [27], as a consequence of the formation of a greater number of oxygen vacancies.

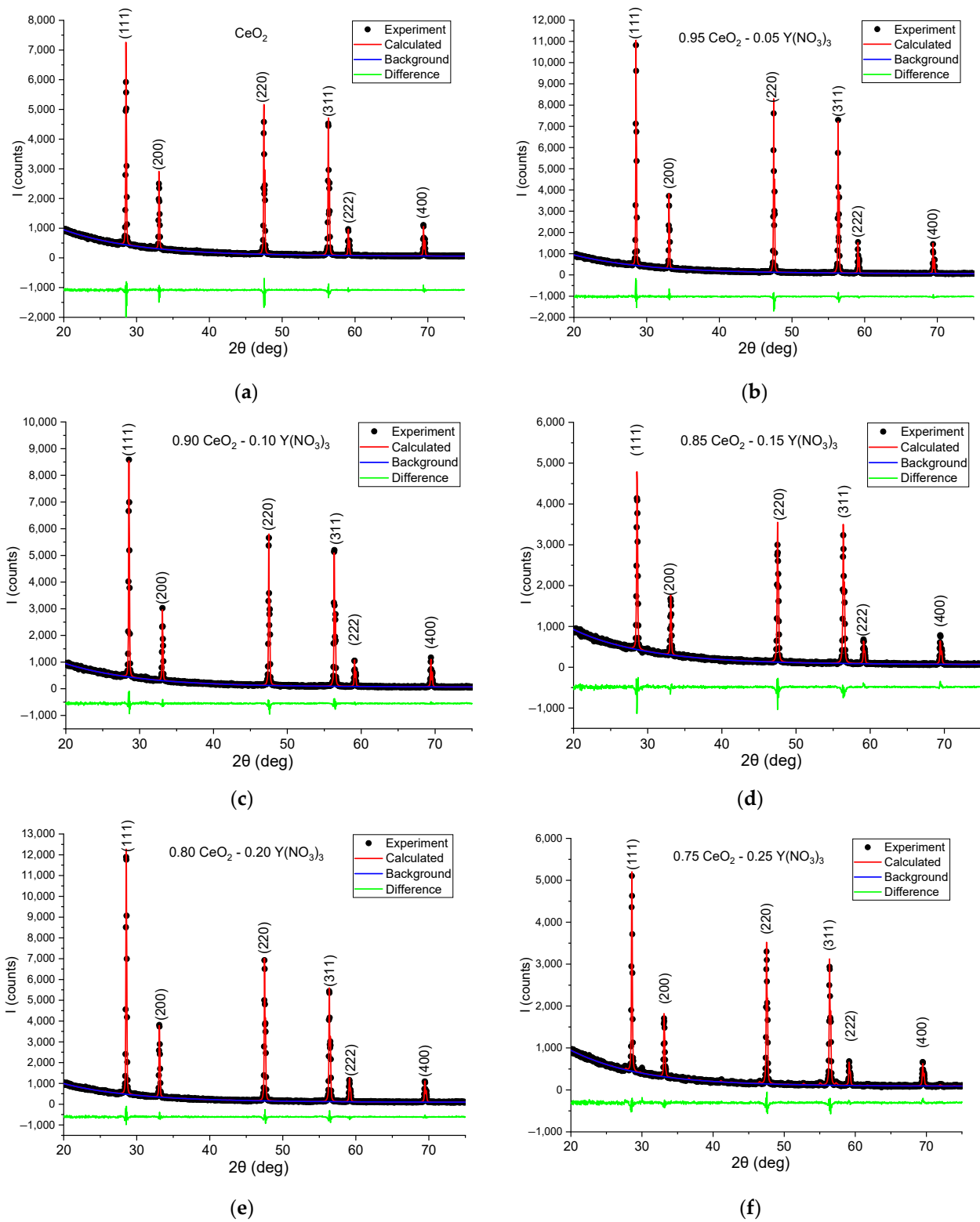


**Figure 1.** Experimental and calculated by the Rietveld refinement method diffraction patterns of synthesized samples: (a)  $x = 0.00$ ; (b)  $x = 0.05$ ; (c)  $x = 0.10$ ; (d)  $x = 0.15$ ; (e)  $x = 0.20$ ; (f)  $x = 0.25$ .

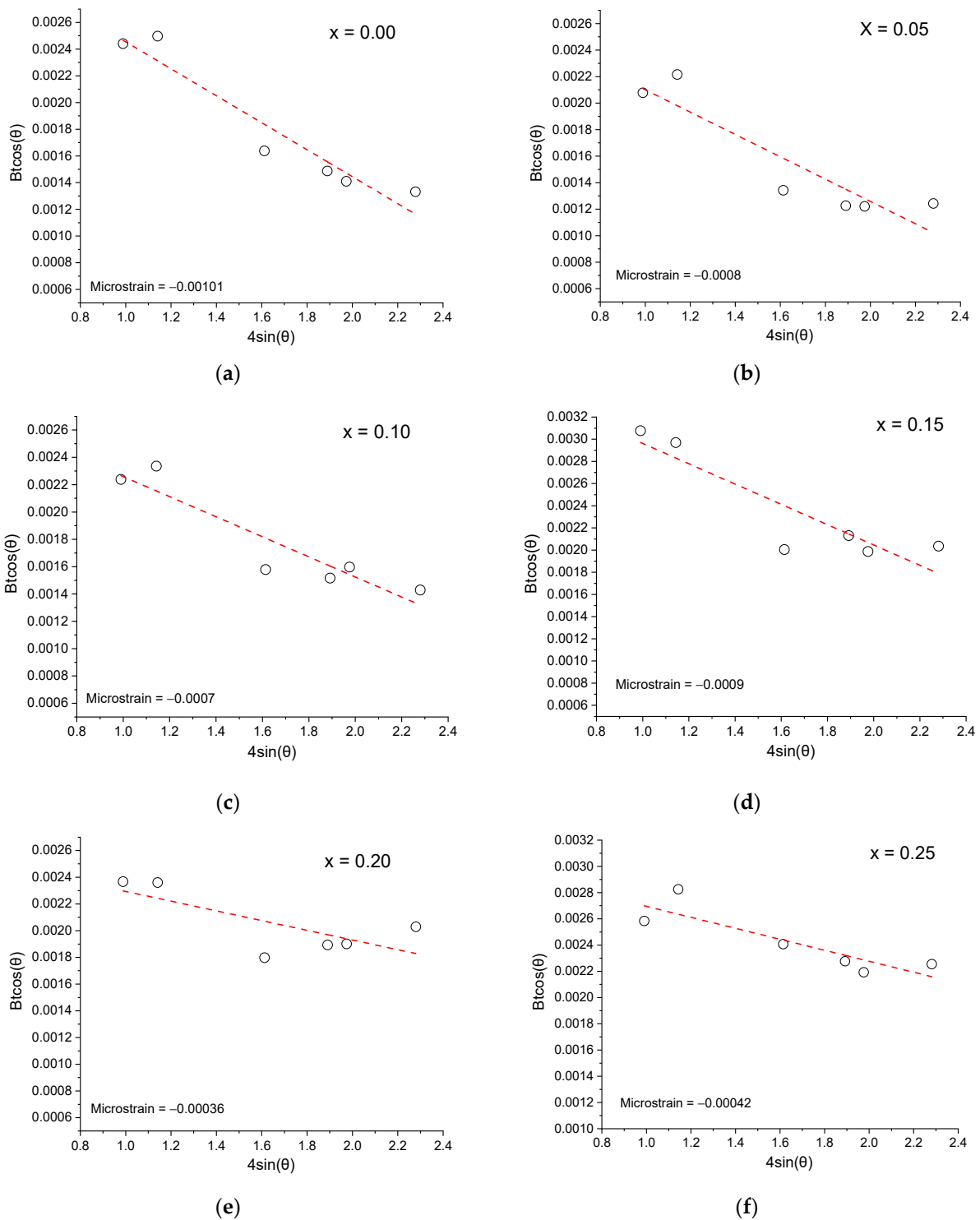


**Figure 2.** Williamson–Hall dependencies calculated from measured diffractograms for synthesized ceramics: (a)  $x = 0.00$ ; (b)  $x = 0.05$ ; (c)  $x = 0.10$ ; (d)  $x = 0.15$ ; (e)  $x = 0.20$ ; (f)  $x = 0.25$ .

SEM and optical microscopy micrographs were used to study the microstructure.

In the case of the experimental samples, it was discovered that the boundaries between grains were particularly well-defined on the surfaces of the annealed tablets. As a result, optical microscopy was performed on the surfaces of the ceramic tablets. The microstructure of the cerium oxide ceramic sample without the addition of  $Y(NO_3)_3$  was similar in the cases of one and two annealings. Figure 3 shows optical micrographs of the tablet surface (left images) and SEM micrographs (right images) of cross-sections of the twice-annealed

tablets. It should be noted that for the undoped sample, the grains have the appearance of irregular polygons, while samples with  $x > 0.00$  have ellipsoidal and round grains. For the cross-sections, the grains have excellent cohesion, which indirectly shows the intensity of sintering processes during synthesis [28].

**Table 2.** Dependence of average crystallite size  $d_{av}$ , dislocation density, and microstresses on dopant concentration.

x	$d_{av}$ , nm	Dislocation Density · 10 <sup>15</sup> , Line per m <sup>2</sup>	Microstrain
0.00	82.1 ± 21.08	0.15	−0.00101 ± 0.00014
0.05	95.1 ± 23.94	0.11	−0.00084 ± 0.00019
0.10	80.7 ± 15.99	0.15	−0.00073 ± 0.00014
0.15	60.7 ± 11.57	0.27	−0.00092 ± 0.00022
0.20	68.2 ± 7.87	0.22	−0.00036 ± 0.00016
0.25	57.7 ± 5.41	0.30	−0.00042 ± 0.00011

In the undoped sample, internal pores within the grains can be observed, which might be responsible for the higher microstrain in the  $x = 0.00$  sample as detected through the Williamson–Hall method. As the concentration  $x$  increases, predominantly intergranular pores are detected within the microstructure. Analysis of optical micrographs of samples subjected to two annealing processes reveals a reduction in grain size upon introducing the dopant into the initial mixture. The decrease in grain size in the synthesized ceramic is attributed to the segregation of the doping Y ions at the grain boundaries. This results in a slower movement of boundaries between neighboring coalescing particles during the sintering process [29], thus preventing the grain growth observed in the undoped sample under the given temperature and time conditions.

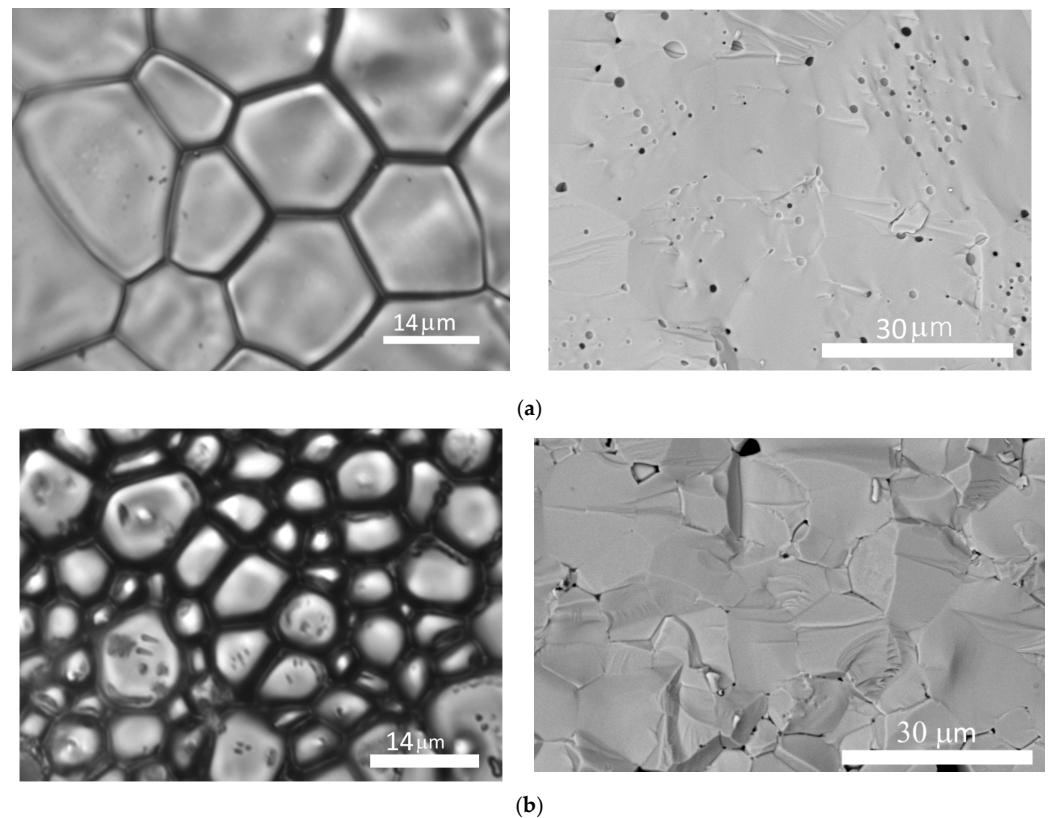


**Figure 3.** Cont.

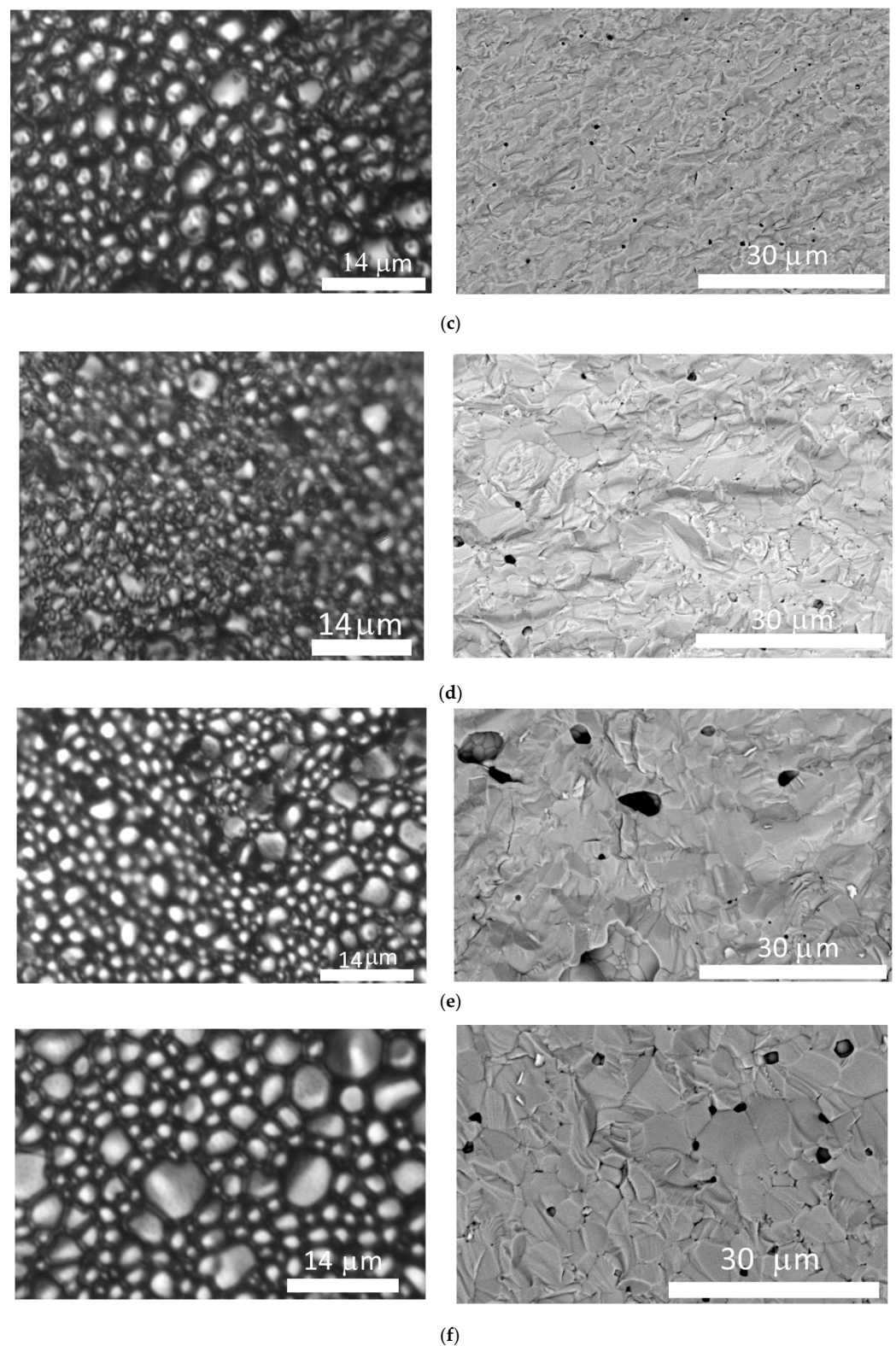


**Figure 3.** Optical micrographs (left) and SEM micrographs of cross sections (right) of samples with two annealings: (a)  $x = 0.00$ ; (b)  $x = 0.05$ ; (c)  $x = 0.10$ ; (d)  $x = 0.15$ ; (e)  $x = 0.20$ ; (f)  $x = 0.25$ .

Micrographs of samples subjected to a single annealing reveal the formation of pores, which occurs due to the decomposition of yttrium nitrate following  $4Y(NO_3)_3 \rightarrow 2Y_2O_3 + 12NO_2 + 3O_2$ . The released nitrogen dioxide and oxygen create macroscopic pores within the microstructure at low dopant concentrations. At higher dopant concentrations, the

merging of macroscopic pores and the formation of a sponge-like structure can be observed. These changes can be traced in the microphotographs presented in Figure 4.

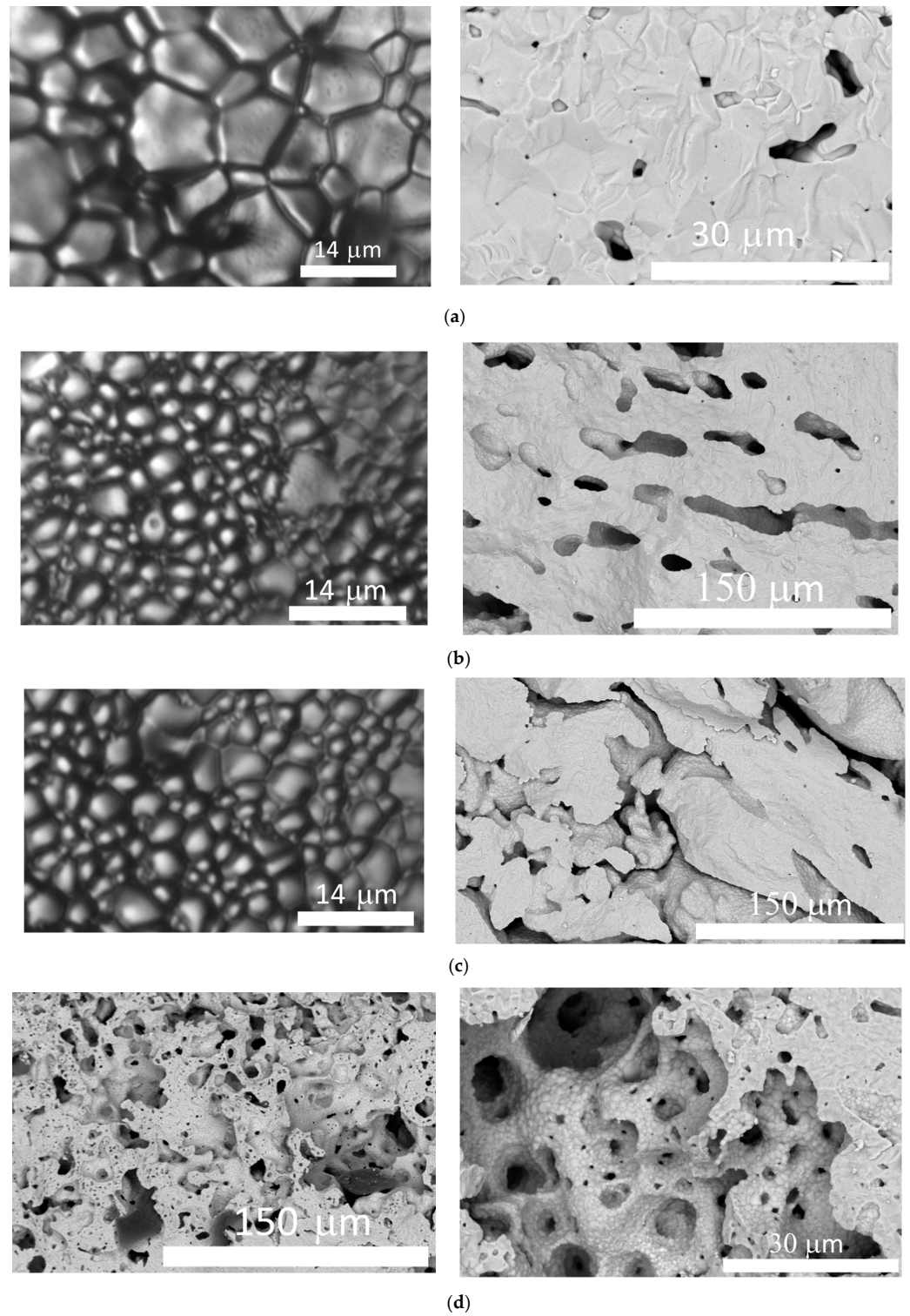
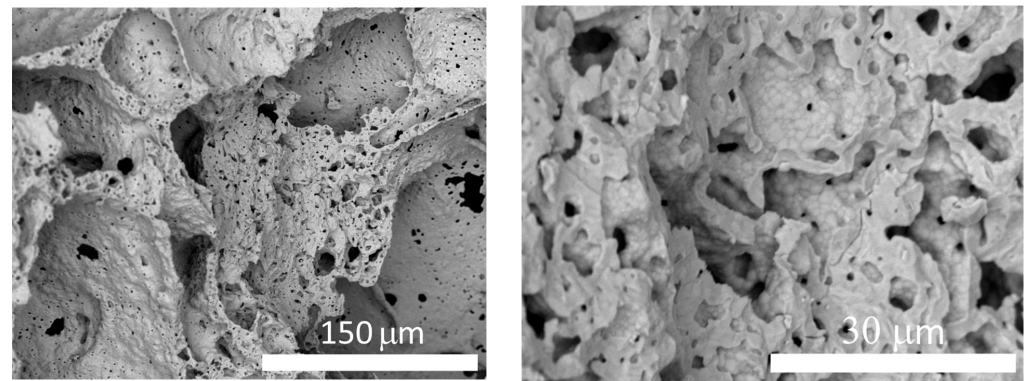


Figure 4. Cont.



(e)

**Figure 4.** Optical micrographs (left, a–c) and SEM micrographs of samples with one annealing: (a)  $x = 0.05$ ; (b)  $x = 0.10$ ; (c)  $x = 0.15$ ; (d)  $x = 0.20$ ; (e)  $x = 0.25$ .

The average grain size was determined using the line intercept method for cases of both one and two annealings based on micrographs obtained from optical microscopy or SEM, utilizing the ImageJ software 1.54f [30]. Figure 5a illustrates the relationship between the average grain size and dopant concentration. It is evident that for  $\text{CeO}_2$  ceramics, the largest grain size is  $27.6 \mu\text{m}$ , whereas for yttrium-doped cerium ceramics with  $x > 0.05$ , the average grain size ranges from  $1.5$  to  $4.2 \mu\text{m}$ . Furthermore, from the graph in Figure 5a, it can also be observed that the formation of pores during annealing can influence the average grain size within the range of  $x = 0.15$ – $0.25$ . The possible explanation of this effect is associated with a high concentration of macropores, which reduce mass transport during solid-state sintering and limit grain growth.

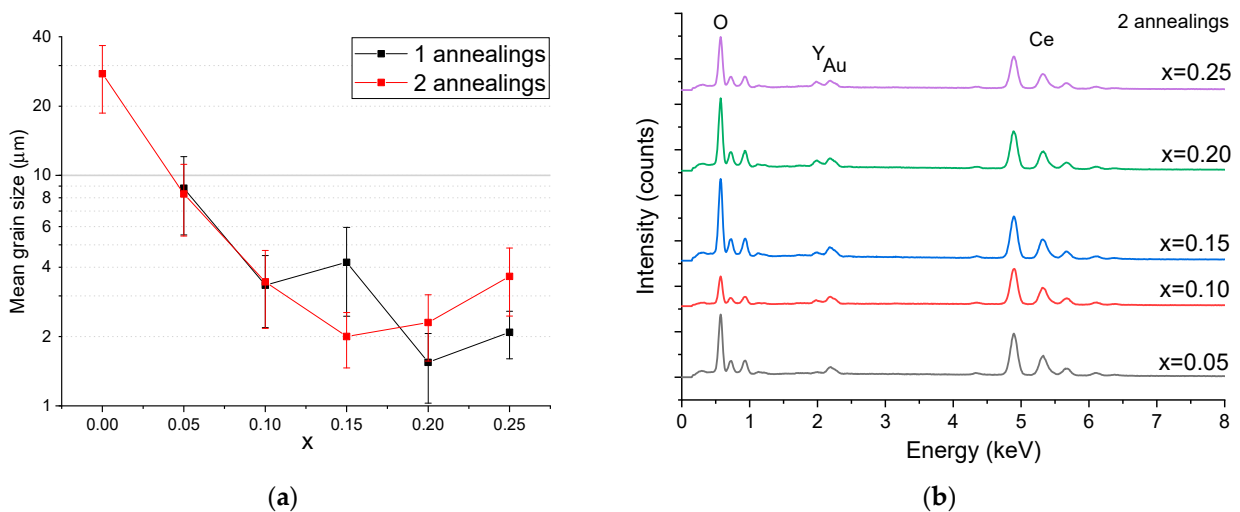


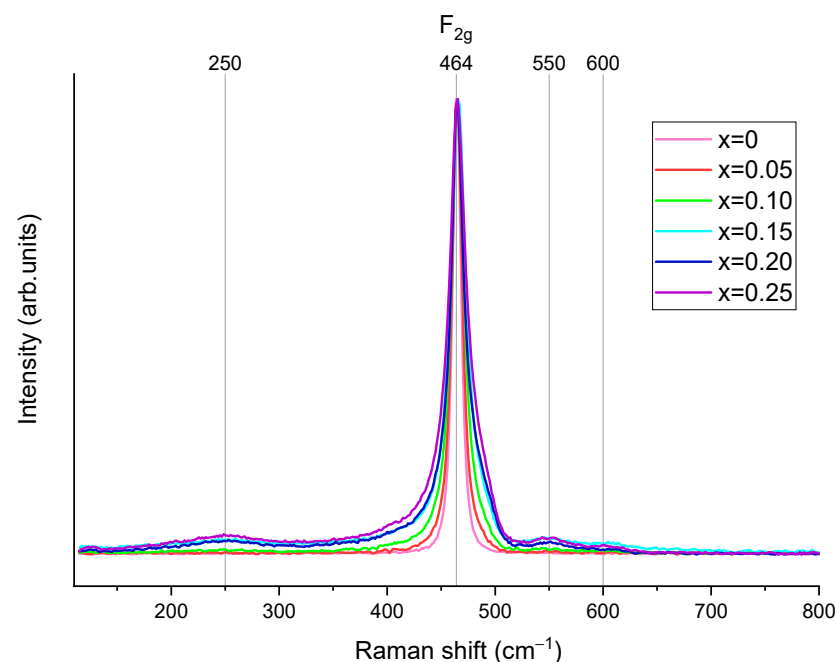
**Figure 5.** Dependence of average grain size on dopant concentration (a) and energy dispersive analysis spectra (b) for the synthesized samples.

Energy-dispersive X-ray analysis (EDX) of cross-sections of experimental samples subjected to two annealings is shown in Figure 5b. The EDX spectra indicate the presence of only Y, Ce, and O elements in all prepared experimental samples. The calculation of the elemental composition based on the obtained spectra is presented in Table 3. The Ce/O ratio in atomic concentrations, considering uncertainties and standard deviations, aligns with the stoichiometry of the experimental samples.

**Table 3.** Results of surface chemical composition analysis via the EDX method.

x	O Concentration, at. %	Ce Concentration, at. %	Y Concentration, at. %
0.00—1 annealing	55.23 ± 4.57	42.77 ± 4.24	-
0.05—1 annealing	52.20 ± 9.64	45.60 ± 9.02	0.46 ± 0.11
0.10—1 annealing	56.25 ± 4.01	39.77 ± 3.75	2.06 ± 0.26
0.15—1 annealing	61.74 ± 10.76	33.79 ± 8.73	2.75 ± 1.41
0.20—1 annealing	55.92 ± 7.08	37.74 ± 7.18	4.39 ± 0.52
0.25—1 annealing	56.99 ± 6.69	35.82 ± 5.82	5.22 ± 0.52
0.05—2 annealings	58.06 ± 6.08	39.50 ± 5.92	0.65 ± 0.28
0.10—2 annealings	41.77 ± 4.81	52.83 ± 4.47	2.53 ± 0.59
0.15—2 annealings	59.12 ± 4.34	37.08 ± 3.88	1.39 ± 0.47
0.20—2 annealings	62.47 ± 2.19	32.19 ± 2.09	3.32 ± 0.48
0.25—2 annealings	52.01 ± 7.54	42.63 ± 6.72	2.58 ± 1.01

The obtained CeO<sub>2</sub> samples with varying Y concentrations were examined using Raman spectroscopy, and the spectra are depicted in Figure 6. The most prominent peak in the spectra, occurring at 464 cm<sup>-1</sup>, corresponds to the triply degenerate optical phonon mode F<sub>2g</sub>, which is characteristic of the cubic fluorite structure of cerium oxide with the O<sub>h</sub><sup>5</sup> spatial group (Fm3m). The high symmetry of the CeO<sub>2</sub> structure, along with the strong polarizability of Ce-O bonds, contributes to the high intensity of the F<sub>2g</sub> mode [31]. This mode is often associated with the symmetric stretching vibrations of Ce-O<sub>8</sub>, yet the force constants of O-O also contribute, and their influence is more significant than that of Ce-O [32].

**Figure 6.** Raman spectra obtained for CeO<sub>2</sub> samples with different Y(NO<sub>3</sub>)<sub>3</sub> concentrations.

In the Raman spectra of pure CeO<sub>2</sub> and with 5 wt.% concentration of Y(NO<sub>3</sub>)<sub>3</sub>, only one peak at 464 cm<sup>-1</sup> related to the F<sub>2g</sub> mode is observed. With the rising concentration of the dopant, the original translational symmetry of the crystal is broken due to the introduction of anion vacancies and other defects. As a result, phonons coming from different regions of the Brillouin zone begin to participate in the formation of optical spectra. This leads to the appearance of many broadened and low-intensity bands in the spectra [16]. At a Y concentration of 10 wt.%, weak and broad peaks appear in the regions of 250, 550, and 600 cm<sup>-1</sup>. The peak at 250 cm<sup>-1</sup> corresponds to the second-order transverse acoustic mode

(2TA) [33]. The modes observed in the 550–600  $\text{cm}^{-1}$  range are typically attributed to the D-band (D is for defects). Its positioning corresponds to the LO mode ( $F_{1u}$  symmetry), arising due to the relaxation of selection rules caused by the lowering of symmetry resulting from the presence of defects [34].

Sometimes, in addition to the D-band around 600  $\text{cm}^{-1}$ , a peak at 1200  $\text{cm}^{-1}$ , attributed to the second harmonic of the longitudinal optical (2LO) mode in the cubic phase, is also observed. However, it is typically enhanced under conditions of resonant Raman scattering, which did not manifest in our experiment. With an increase in the Y concentration, a slight growth of these peaks is observed, indicating the formation of oxygen vacancies. The appearance of the peak at 550  $\text{cm}^{-1}$  is linked to oxygen vacancies, acting as charge compensation defects, ensuring charge neutrality upon  $\text{CeO}_2$  doping when  $\text{Y}^{3+}$  ions replace  $\text{Ce}^{4+}$  ions [35,36]. The peak at 600  $\text{cm}^{-1}$  is also attributed to oxygen vacancies, which arise as  $\text{Ce}^{4+}$  is reduced to  $\text{Ce}^{3+}$  [17].

Table 4 shows the change in the full width at half maximum (FWHM) of the  $F_{2g}$  peak as the concentration of  $\text{Y}(\text{NO}_3)_3$  increases. The broadening of this peak can be attributed to both a reduction in crystallite size and the formation of defects [37,38].

**Table 4.** Changes in  $F_{2g}$  mode peak parameters for  $\text{CeO}_2$  samples with the increasing concentration of  $\text{Y}(\text{NO}_3)_3$ .

x	Center	FWHM
0	464.44	8.62
0.05	464.82	10.80
0.10	465.31	14.27
0.15	465.80	18.17
0.20	465.23	18.35
0.25	465.46	22.79

The electrical properties of the obtained samples were investigated using dielectric spectroscopy. Figures 7 and 8 depict the frequency-dependent behaviors of the real part of the permittivity ( $\epsilon'$ ) and the dielectric loss tangent ( $\tan \delta$ ) within the frequency range from 100 Hz to 220 kHz for samples annealed twice and once, respectively. For the undoped  $\text{CeO}_2$  sample, it was observed that the permittivity ( $\epsilon'$ ) remains constant at a value of 18.5 with increasing frequency, while the dielectric loss tangent ( $\tan \delta$ ) is  $\sim 7 \times 10^{-4}$ . This value is lower than that calculated and measured in the study [39] due to the porosity of the sample. The low value of the dielectric loss tangent is attributed to the high crystalline perfection of the crystallites and the largest grain size in the  $x = 0.00$  sample [40]. Indirect confirmation of this was provided via X-ray and Raman analysis of the peaks. With an increase in dopant concentration, permittivity and dielectric losses also increase. Frequency dispersion appears in the low-frequency range of the spectrum in the dielectric characteristics' frequency dependencies. However, it can be noted that for samples annealed once at concentrations of  $x = 0.20$  and  $0.25$ , the permittivity significantly decreases compared to other samples.

A comparison of the dependencies of permittivity at low frequency (100 Hz) and high frequency (10 kHz) on dopant concentration and the number of annealing cycles for all samples is presented in Figure 9a,b. It is well known that several factors influence the value of ceramic permittivity, such as the ceramic's chemical composition, the perfection of the crystalline lattice, and microstructure characteristics (porosity, grain size). To explain the changes in the electrical properties of the synthesized samples, the influence of chemical composition and defects in the crystalline lattice should be primarily considered. The increase in low-frequency  $\epsilon'$  values (and the appearance of low-frequency permittivity dispersion) with an increase in  $x$  is primarily associated with the influence of through-ion conduction [41,42]. This type of conductivity arises during the substitution of  $\text{Ce}^{4+}$  ions with  $\text{Y}^{3+}$  ions, leading to the formation of oxygen vacancies in the crystalline lattice. For the same reason, low-frequency dielectric losses increase. Upon substitution, the concentration of point defects and the mobility of charged particles interacting with vacancies

increase, enhancing ionic conductivity. However, this effect is limited by vacancy–vacancy interactions at concentrations of  $x$  greater than 0.15 [21].

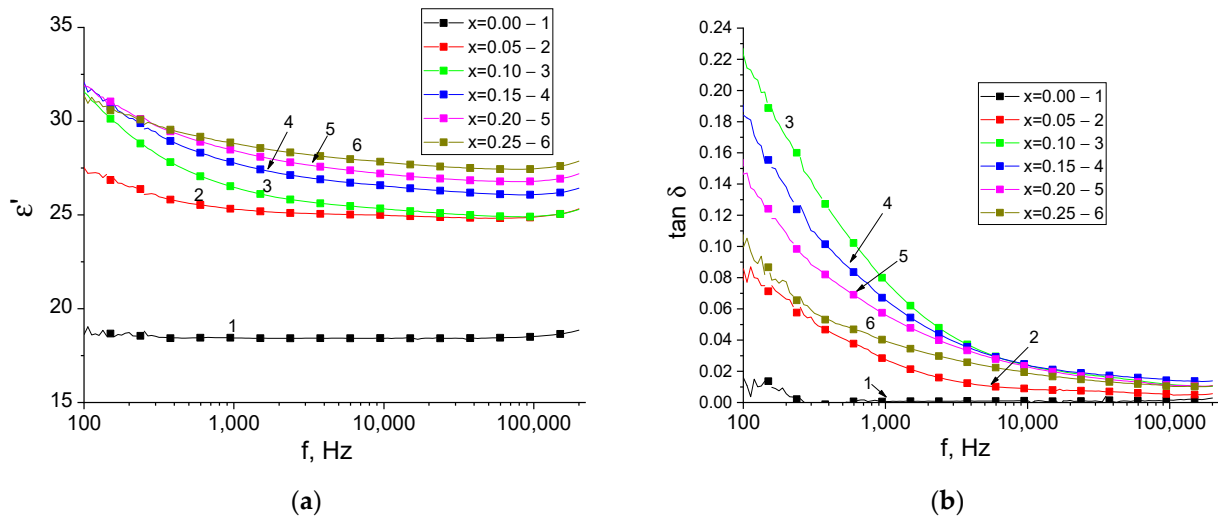


**Figure 7.** Frequency dependencies of permittivity (a) and dielectric loss tangents (b) for samples obtained with two annealings.

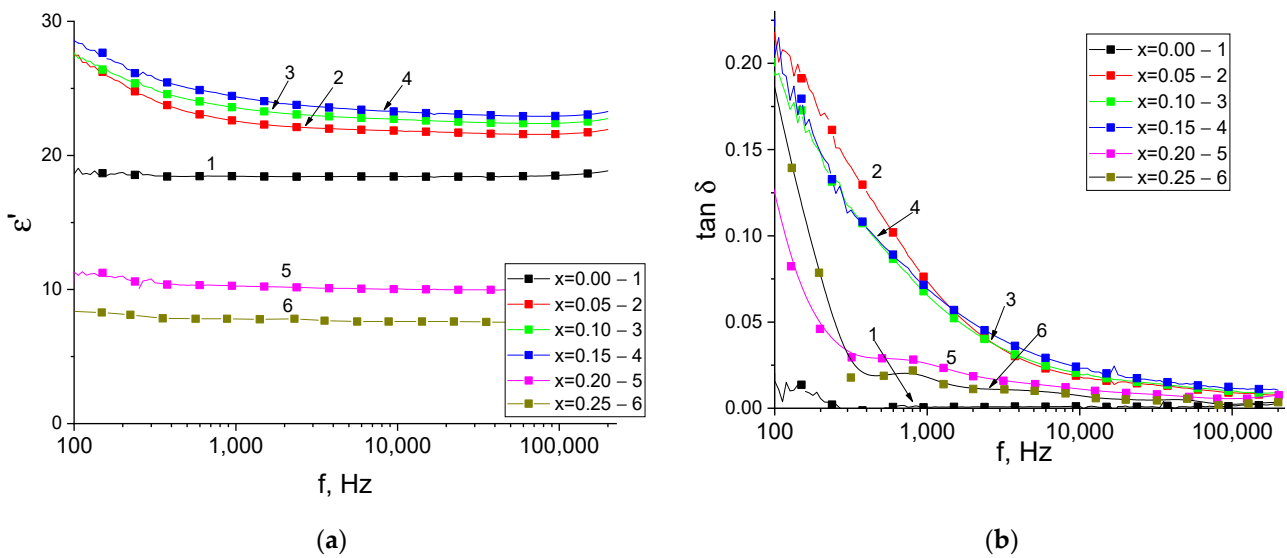


**Figure 8.** Frequency dependencies of permittivity (a) and dielectric loss tangents (b) for samples obtained with one annealing.

Further, it is important to consider the characteristics of the microstructure that can significantly influence the  $\epsilon'(f)$  spectrum. The dispersion of the permittivity is associated with the emergence of polarons in the crystalline lattice, as well as interface polarization at the grain/grain boundary interfaces [43–45].

The latter phenomenon is possible because the conductivity increases within the grains, while the grain boundaries remain insulating, creating conditions for charge accumulation at the interface. Thus, the increase in low-frequency  $\epsilon'$  with the rise in  $x$  up to 0.15 in samples subjected to two annealings is associated with changes in the ceramic’s conductivity. This can also be confirmed by examining the calculated values of electrical conductivity at low frequency (Figure 9c). Up to a concentration of  $x = 0.10$ , a sharp increase in  $\sigma_{AC}$  is observed with a tenfold rise in dopant concentration. With further increases in  $x$ , the conductivity remains higher than in the non-substituted sample. In samples subjected to a single annealing process, the growth of low-frequency  $\epsilon'$  is limited by high porosity.

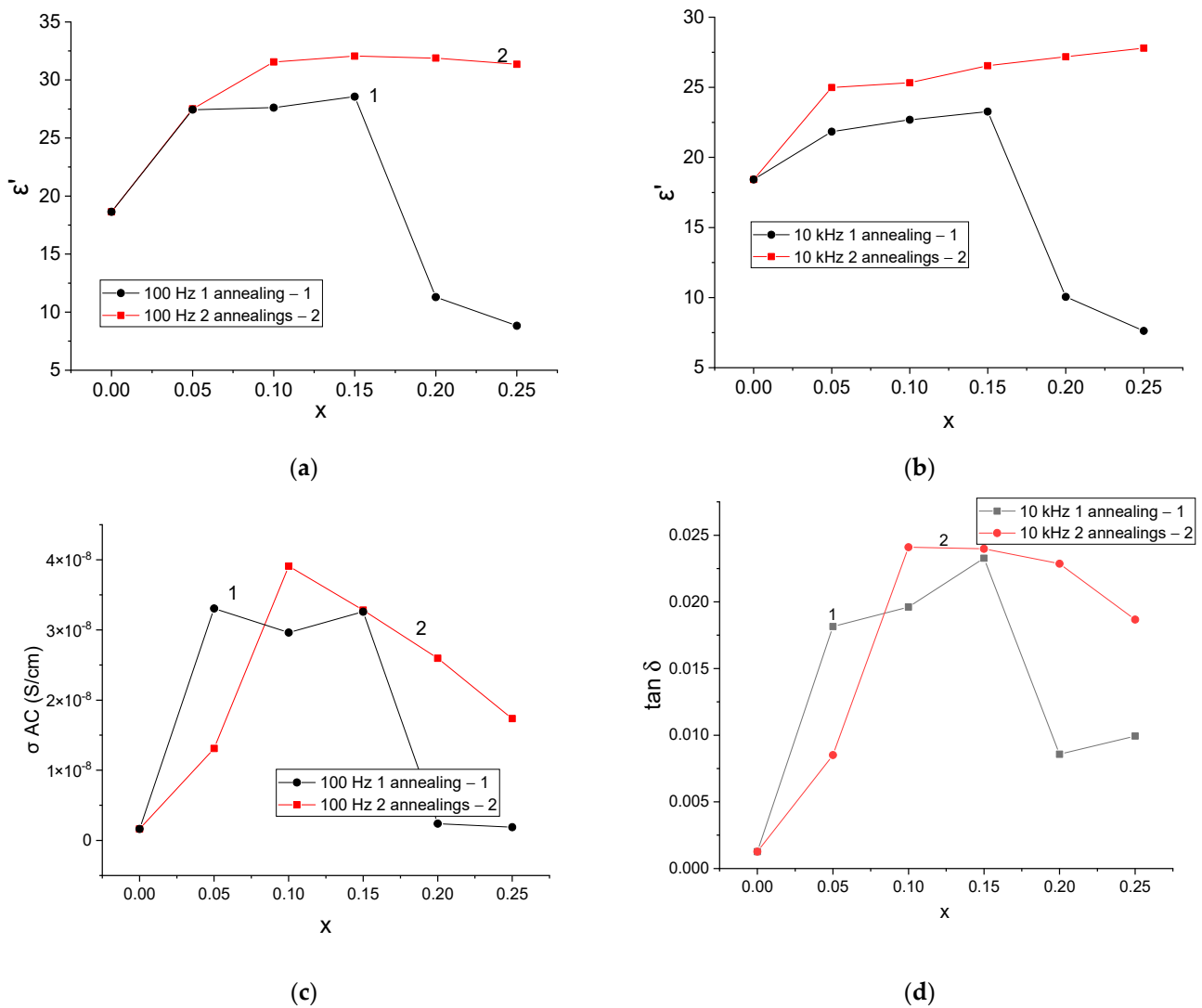


**Figure 9.** Dependences of permittivity on dopant concentration at 100 Hz (a), 10 kHz (b), AC conductivity at 100 Hz (c), and dielectric loss tangent on dopant concentration at 10 kHz (d).

When considering the variation of high-frequency dielectric permittivity from dopant concentration, an increase in  $\epsilon'$  values with increasing  $x$  is also observed for the sample with two annealings. However, in this case, the increase is not related to a change in the ionic conductivity of the ceramics. Since the cubic lattice parameter decreases with increasing dopant concentration, the unit cell volume also decreases. According to the Clausius–Mossotti relation [46], a decrease in the lattice volume can increase the dielectric constant of oxides. Thus, in Y substituted stabilized zirconia ceramics, the dielectric permittivity can increase from 23 to 40 with the stabilization of the tetragonal phase and the reduction of the lattice volume by 5% [47].

Moreover, the addition of dopants can increase the polarizability of ions in the oxide crystal lattice. The dependence of dielectric losses on  $x$  of both series of samples at 10 kHz is shown in Figure 9d. In the case of one annealing and two annealings, the dielectric losses in the obtained samples increase with the increasing concentration of  $Y(NO_3)_3$  in the initial charge up to concentrations  $x = 0.10$ – $0.15$ . The increased values of  $\tan \delta$  in the substituted  $CeO_2$ -Y ceramics are associated with an increase in the defect concentration, which was detected through X-ray diffraction analysis and Raman studies of the obtained samples.

The mechanical properties of the synthesized ceramics were evaluated by measuring the microhardness using the Vickers method with a load of 0.2 kgf (HV0.2). The results

of the measurements are shown in Figure 10a. In the case of samples obtained with one annealing, the microhardness reaches its maximum at a dopant concentration of 0.05, then decreases to the values of the undoped sample. For this series, microhardness measurements could not be made for samples with concentrations  $x = 0.20$  and  $0.25$  because the porous structure of the ceramic could not withstand the indentation load. For the series of samples with two annealings, an increase in microhardness values was observed with increasing  $Y(NO_3)_3$  concentration up to a dopant concentration of  $0.20$ . In both cases, the decrease in HV0.2 values correlates with the change in density and porosity (Figure 10b,c).

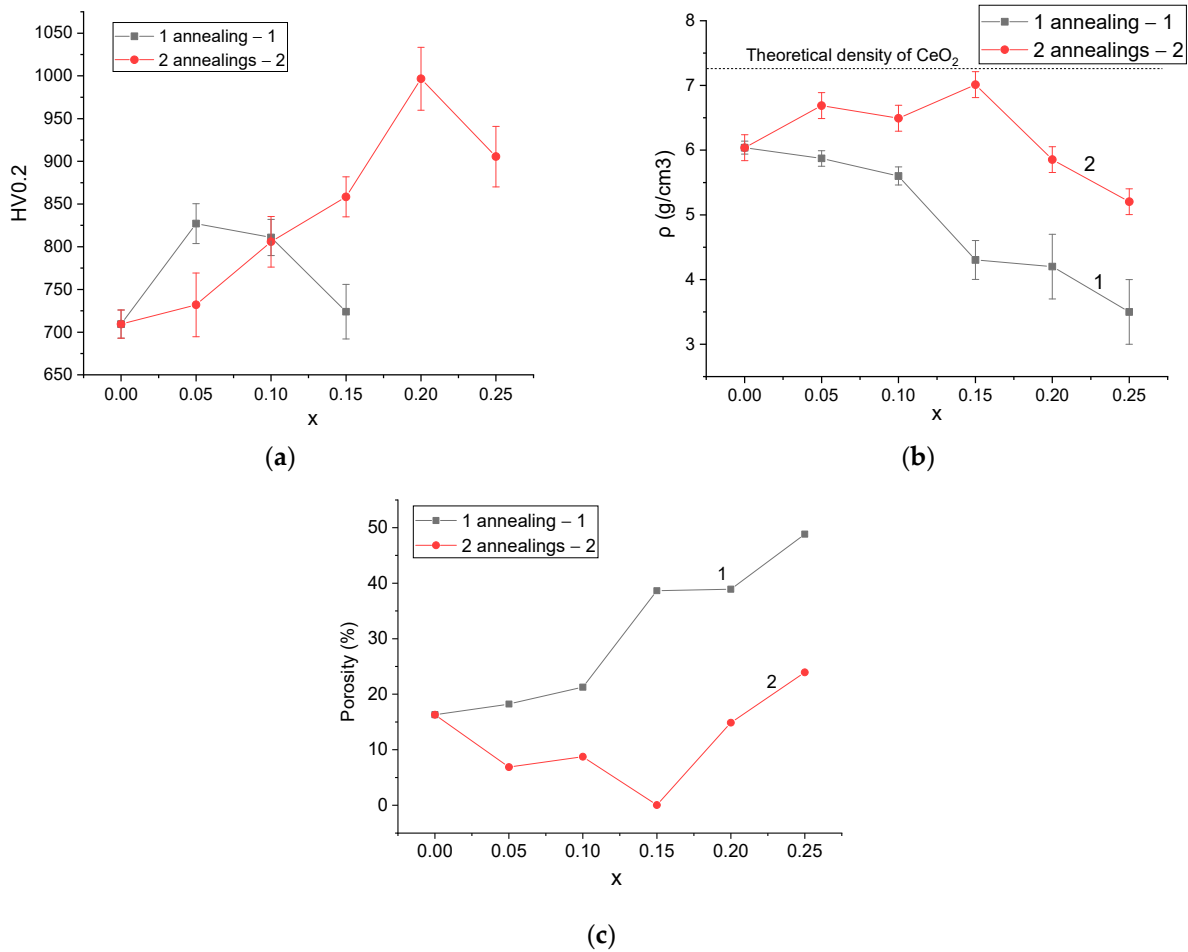


**Figure 10.** Dependence of HV0.2 microhardness (a), apparent density (b), and porosity (c) on dopant concentration.

For all the samples, the apparent density and porosity were calculated using the X-ray density values (Table 1). The highest HV0.2 value was obtained for the least porous sample, which demonstrates a pronounced dependence of microhardness on the presence of pores in the sample [48,49]. On the other hand, despite the decrease in apparent density (increase in porosity), in some cases, it was observed that microhardness does not follow the change in apparent density (e.g., sample with two annealings and concentration  $x = 0.2$ ). In this case, the increasing value of HV0.2 may be due to the small value of the average grain size as well as the high concentration of dislocations. In large grains, mechanical stresses can propagate along dislocations over longer distances than in the case of small grains [50]. The propagation of mechanical stresses stops at grain boundaries, which causes the hardening of ceramics. In addition, similar to metals, hardening can be affected by a high concentration of dislocations, the values of which are maximum for samples with high dopant content.

The experimental results show that the sintering of Y-doped CeO<sub>2</sub> ceramics from charge containing Y(NO<sub>3</sub>)<sub>3</sub> nitrate is of practical interest in the field of energy. In previous work that was dedicated to the possibility of the application of non-porous doped ceria ceramics in electrochemical devices, complex investigations were conducted [51]. By comparison, the data obtained from this work with [51] indicate that porous ceria ceramics have comparable microhardness (805.6–860.6) and grain size (3–6 μm). As mentioned before, high-temperature ionic conductivity in ceramics for fuel cells should be in the order of  $1 \times 10^{-3}$  to  $8 \times 10^{-2}$  S/cm. In this work, high-temperature measurements of electrical properties were not carried out, but room-temperature results are also promising. First, significant improvements in the electrical properties of ceramics with 1 annealing and 2 annealings were found. Second, substitution of Ce<sup>4+</sup> by Y<sup>3+</sup> was also confirmed via XRD, Raman spectroscopy, and dielectric measurements, which are necessary for improving oxygen conductivity. If functional elements made of porous materials are required in the production of, for example, solid oxide fuel cells or hydrogen separation systems, the one-stage annealing process proposed in this work can be applied to create such materials. At concentrations of  $x = 0.05$ – $0.15$ , samples fabricated with a single annealing process (porosity 15–20%) had values of low-frequency electrical conductivity (at room temperature)  $\sim 3 \times 10^{-8}$  S/cm, dielectric constant  $\sim 27$ , and microhardness HV0.2 in the range of 700–825. In less porous samples fabricated with two annealings, these values were higher by 20–30% with porosity of 1–8%. Regardless of the annealing variants, doping CeO<sub>2</sub> with Y ions leads to an increase in the ionic conductivity, permittivity, and microhardness, which improves the functional and performance characteristics of ceramics made from cerium oxide.

#### 4. Conclusions

In this study, CeO<sub>2</sub> ceramic samples with Ce<sup>4+</sup> substitution for Y<sup>3+</sup> were successfully synthesized via the solid-phase method with one and two annealing steps. The impact of the dopant concentration (ranging from 0.00 to 0.25) on the structural, dielectric, and mechanical properties of the cerium oxide ceramics was investigated using various techniques: powder X-ray diffraction; Raman spectroscopy; microhardness measurements; and dielectric spectroscopy. The findings reveal a substantial influence of the dopant concentration on the sample morphology, lattice parameter, electrical conductivity, dielectric constant, and HV microhardness. Notably, the substitution of Ce<sup>4+</sup> ions with Y<sup>3+</sup> led to a decrease in the lattice parameter from 5.411094 to 5.406372 Å. This phenomenon is attributed to the presence of oxygen vacancies, which maintain the crystal's electroneutrality.

In addition, X-ray structural analysis and Raman spectroscopy showed that with increasing dopant concentration, the crystallite size decreased, and the defect density within the crystalline structure increased. Scanning electron microscopy (SEM) and optical microscopy images indicated a reduction in the average grain size of ceramics with high substitution levels from 27.6 to 3.5 μm. Doping CeO<sub>2</sub> with yttrium ions led to an increase in the low-frequency dielectric constant from 18 to 32 for the series of samples subjected to two annealings, and from 18 to 27 for the series with a single annealing. Furthermore, a concentration-dependent trend in low-frequency electrical conductivity was observed across the investigated concentration range. This trend exhibited a maximum where samples subjected to two annealing processes demonstrated the highest conductivity at  $3.9 \times 10^{-8}$  Sm/m, while porous samples with one annealing exhibited a conductivity of  $3.3 \times 10^{-8}$  Sm/m. Despite having a porosity of 20%, the samples subjected to a single annealing process showed only a  $\sim 20\%$  reduction in microhardness (HV0.2), which is close to the microhardness of the undoped sample.

In summary, it was determined that using a single annealing process during the solid-phase synthesis of yttrium nitrate-doped ceramics (with weight concentrations ranging from 0.05 to 0.15) enables the production of porous samples with favorable mechanical and electrical properties for practical applications in the field of energy.

**Author Contributions:** Conceptualization, R.I.S., N.O.V., Y.A.G., D.I.S., M.V.Z., D.B.B. and A.L.K.; methodology, R.I.S., N.O.V., Y.A.G., D.I.S., M.V.Z., D.B.B. and A.L.K.; formal analysis, R.I.S., N.O.V., Y.A.G., D.I.S., M.V.Z., D.B.B. and A.L.K.; investigation, R.I.S., N.O.V., Y.A.G., D.I.S., M.V.Z., D.B.B. and A.L.K.; resources, A.L.K.; writing—original draft preparation, review, and editing, R.I.S., N.O.V. and Y.A.G.; visualization, A.L.K.; supervision, A.L.K. All authors have read and agreed to the published version of the manuscript.

**Funding:** This research was funded by the Science Committee of the Ministry of Education and Science of the Republic of Kazakhstan (No. BR11765580).

**Institutional Review Board Statement:** Not applicable.

**Informed Consent Statement:** Not applicable.

**Data Availability Statement:** Not applicable.

**Conflicts of Interest:** The authors declare no conflict of interest.

## References

1. Middleburgh, S.C.; Lee, W.E.; Rushton, M.J.D. Ceramics in the nuclear fuel cycle. In *Advanced Ceramics for Energy Conversion and Storage*; Guillon, O., Ed.; Elsevier Series on Advanced Ceramic Materials; Woodhead Publishing Limited: Sawston, UK, 2019; ISBN 978-0-08-102784-4.
2. Mistarihi, Q.M.; Raj, V.; Kim, J.H.; Ryu, H.J. Thermal Conductivity of Mo-Reinforced ZrO<sub>2</sub> Composites Fabricated by Spark Plasma Sintering for Inert Matrix Fuels. *Mater. Des.* **2017**, *134*, 476–485. [[CrossRef](#)]
3. Degueldre, C.; Paratte, J.M. Concepts for an Inert Matrix Fuel, an Overview. *J. Nucl. Mater.* **1999**, *274*, 1–6. [[CrossRef](#)]
4. Momin, N.; Manjanna, J.; Kobayashi, S.; Aruna, S.T.; Senthil Kumar, S.; Nayaka, G.P. Synthesis and Ionic Conductivity of Calcium-Doped Ceria Relevant to Solid Oxide Fuel Cell Applications. *Mater. Adv.* **2022**, *3*, 8780–8791. [[CrossRef](#)]
5. Meng, Q.-L.; Lee, C.; Ishihara, T.; Kaneko, H.; Tamaura, Y. Reactivity of CeO<sub>2</sub>-Based Ceramics for Solar Hydrogen Production via a Two-Step Water-Splitting Cycle with Concentrated Solar Energy. *Int. J. Hydrogen Energy* **2011**, *36*, 13435–13441. [[CrossRef](#)]
6. Choi, J.; Yeon, J.H.; Yook, S.H.; Shin, S.; Kim, J.Y.; Choi, M.; Jang, S. Multifunctional Nafion/CeO<sub>2</sub> Dendritic Structures for Enhanced Durability and Performance of Polymer Electrolyte Membrane Fuel Cells. *ACS Appl. Mater. Interfaces* **2021**, *13*, 806–815. [[CrossRef](#)]
7. Nelson, A.T.; Rittman, D.R.; White, J.T.; Dunwoody, J.T.; Kato, M.; McClellan, K.J. An Evaluation of the Thermophysical Properties of Stoichiometric CeO<sub>2</sub> in Comparison to UO<sub>2</sub> and PuO<sub>2</sub>. *J. Am. Ceram. Soc.* **2014**, *97*, 3652–3659. [[CrossRef](#)]
8. Suzuki, K.; Kato, M.; Sunaoshi, T.; Uno, H.; Carvajal-Nunez, U.; Nelson, A.T.; McClellan, K.J. Thermal and Mechanical Properties of CeO<sub>2</sub>. *J. Am. Ceram. Soc.* **2018**, *102*, 1994–2008. [[CrossRef](#)]
9. Frieß, F.; Liebert, W. Inert-Matrix Fuel for Transmutation: Selected Mid- and Long-Term Effects on Reprocessing, Fuel Fabrication and Inventory Sent to Final Disposal. *Prog. Nucl. Energy* **2022**, *145*, 104106. [[CrossRef](#)]
10. Kozlovskiy, A.L.; Zdorovets, M.V.; Shlimas, D.I. Study of the Morphological and Structural Features of Inert Matrices Based on ZrO<sub>2</sub>-CeO<sub>2</sub> Doped with Y<sub>2</sub>O<sub>3</sub> and the Effect of Grain Sizes on the Strength Properties of Ceramics. *Metals* **2022**, *12*, 1687. [[CrossRef](#)]
11. Zhang, T.; Ma, J.; Kong, L.; Chan, S.; Kilner, J. Aging Behavior and Ionic Conductivity of Ceria-Based Ceramics: A Comparative Study. *Solid State Ion.* **2004**, *170*, 209–217. [[CrossRef](#)]
12. Eguchi, K.; Setoguchi, T.; Inoue, T.; Arai, H. Electrical Properties of Ceria-Based Oxides and Their Application to Solid Oxide Fuel Cells. *Solid State Ion.* **1992**, *52*, 165–172. [[CrossRef](#)]
13. Zhao, K.; Du, Y. Calcium-Doped Ceria Materials for Anode of Solid Oxide Fuel Cells Running on Methane Fuel. *J. Power Sources* **2017**, *347*, 79–85. [[CrossRef](#)]
14. Grover, V.; Tyagi, A.K. Phase Relations, Lattice Thermal Expansion in CeO<sub>2</sub>-Gd<sub>2</sub>O<sub>3</sub> System, and Stabilization of Cubic Gadolinia. *Mater. Res. Bull.* **2004**, *39*, 859–866. [[CrossRef](#)]
15. Nakajima, A.; Yoshihara, A.; Ishigame, M. Defect-Induced Raman Spectra in doped CeO<sub>2</sub>. *Phys. Rev. B* **1994**, *50*, 13297–13307. [[CrossRef](#)]
16. Mandal, B.P.; Grover, V.; Roy, M.; Tyagi, A.K. X-ray Diffraction and Raman Spectroscopic Investigation on the Phase Relations in Yb<sub>2</sub>O<sub>3</sub>- and Tm<sub>2</sub>O<sub>3</sub>-Substituted CeO<sub>2</sub>. *J. Am. Ceram. Soc.* **2007**, *90*, 2961–2965. [[CrossRef](#)]
17. Souza, E.C.C.; Brito, H.F.; Muccillo, E.N.S. Optical and Electrical Characterization of Samaria-Doped Ceria. *J. Alloys Compd.* **2010**, *491*, 460–464. [[CrossRef](#)]
18. Bhosale, R.R.; Takalkar, G.; Sutar, P.; Kumar, A.; AlMomani, F.; Khraisheh, M. A Decade of Ceria Based Solar Thermochemical H<sub>2</sub>O/CO<sub>2</sub> Splitting Cycle. *Int. J. Hydrogen Energy* **2019**, *44*, 34–60. [[CrossRef](#)]
19. Melchionna, M.; Trovarelli, A.; Fornasiero, P. Synthesis and properties of cerium oxide-based materials. In *Cerium Oxide (CeO<sub>2</sub>): Synthesis, Properties and Applications*; Scire, S., Palmisano, L., Eds.; Metal Oxides Series; Elsevier Science: Amsterdam, The Netherlands, 2019; ISBN 978-0-12-815662-9.

20. Doebelin, N.; Kleeberg, R. Profex: A Graphical User Interface for the Rietveld Refinement programBGMN. *J. Appl. Crystallogr.* **2015**, *48*, 1573–1580. [[CrossRef](#)]
21. Burbano, M.; Norberg, S.T.; Hull, S.; Eriksson, S.G.; Marrocchelli, D.; Madden, P.A.; Watson, G.W. Oxygen Vacancy Ordering and the Conductivity Maximum in Y<sub>2</sub>O<sub>3</sub>-Doped CeO<sub>2</sub>. *Chem. Mater.* **2011**, *24*, 222–229. [[CrossRef](#)]
22. Kim, N.; Stebbins, J.F. Vacancy and Cation Distribution in Yttria-Doped Ceria: An 89Y and 17O MAS NMR Study. *Chem. Mater.* **2007**, *19*, 5742–5747. [[CrossRef](#)]
23. Sánchez-Santolino, G.; Salafranca, J.; Pantelides, S.T.; Pennycook, S.J.; León, C.; Varela, M. Localization of Yttrium Segregation within YSZ Grain Boundary Dislocation Cores. *Phys. Status Solidi A* **2018**, *215*, 1800349. [[CrossRef](#)]
24. Nath, D.; Singh, F.; Das, R. X-ray Diffraction Analysis by Williamson-Hall, Halder-Wagner and Size-Strain Plot Methods of CdSe Nanoparticles- a Comparative Study. *Mater. Chem. Phys.* **2020**, *239*, 122021. [[CrossRef](#)]
25. Rupp, J.L.M.; Infortuna, A.; Gauckler, L.J. Microstrain and Self-Limited Grain Growth in Nanocrystalline Ceria Ceramics. *Acta Mater.* **2006**, *54*, 1721–1730. [[CrossRef](#)]
26. Kurian, M.; Kunjachan, C. Investigation of Size Dependency on Lattice Strain of Nanoceria Particles Synthesised by Wet Chemical Methods. *Int. Nano Lett.* **2014**, *4*, 73–80. [[CrossRef](#)]
27. Tholkappiyar, R.; Vishista, K. Combustion Synthesis of Mg–Er Ferrite Nanoparticles: Cation Distribution and Structural, Optical, and Magnetic Properties. *Mater. Sci. Semicond. Process.* **2015**, *40*, 631–642. [[CrossRef](#)]
28. Rahaman, M.N. *Sintering of Ceramics*; CRC Press: Boca Raton, FL, USA, 2007; ISBN 978-0-8493-7286-5.
29. Boch, P.; Leriche, A. Sintering and microstructure of ceramics. In *Ceramic Materials: Processes, Properties, and Applications*; Boch, P., Ni, J.C., Eds.; John Wiley & Sons: Hoboken, NJ, USA, 2010.
30. Rueden, C.T.; Schindelin, J.; Hiner, M.C.; DeZonia, B.E.; Walter, A.E.; Arena, E.T.; Eliceiri, K.W. ImageJ2: ImageJ for the next Generation of Scientific Image Data. *BMC Bioinform.* **2017**, *18*, 529. [[CrossRef](#)]
31. Mochizuki, S. Infrared Optical Properties of Cerium Dioxide. *Phys. Status Solidi B* **1982**, *114*, 189–199. [[CrossRef](#)]
32. Shimanouchi, T.; Tsuboi, M.; Miyazawa, T. Optically Active Lattice Vibrations as Treated by the GF-Matrix Method. *J. Chem. Phys.* **1961**, *35*, 1597–1612. [[CrossRef](#)]
33. Daniel, M.; Loridant, S. Probing Reoxidation Sites Byin situ Raman Spectroscopy: Differences between Reduced CeO<sub>2</sub>and Pt/CeO<sub>2</sub>. *J. Raman Spectrosc.* **2012**, *43*, 1312–1319. [[CrossRef](#)]
34. Taniguchi, T.; Watanabe, T.; Sugiyama, N.; Subramani, A.K.; Wagata, H.; Matsushita, N.; Yoshimura, M. Identifying Defects in Ceria-Based Nanocrystals by UV Resonance Raman Spectroscopy. *J. Phys. Chem. C* **2009**, *113*, 19789–19793. [[CrossRef](#)]
35. Acharya, S.A.; Gaikwad, V.M.; D’Souza, S.W.; Barman, S.R. Gd/Sm Dopant-Modified Oxidation State and Defect Generation in Nano-Ceria. *Solid State Ion.* **2014**, *260*, 21–29. [[CrossRef](#)]
36. McBride, J.R.; Hass, K.C.; Poindexter, B.D.; Weber, W.H. Raman and X-Ray Studies of Ce<sub>1-x</sub>RE<sub>x</sub>O<sub>2-y</sub>, Where RE = La, Pr, Nd, Eu, Gd, and Tb. *J. Appl. Phys.* **1994**, *76*, 2435–2441. [[CrossRef](#)]
37. Kosacki, I.; Suzuki, T.; Petrovsky, V.; Anderson, H.U.; Colombari, P. Lattice Defects in Nanocrystalline CeO<sub>2</sub>thin Films. *Radiat. Eff. Defects Solids* **2001**, *156*, 109–115. [[CrossRef](#)]
38. Filtschew, A.; Hofmann, K.; Hess, C. Ceria and Its Defect Structure: New Insights from a Combined Spectroscopic Approach. *J. Phys. Chem. C* **2016**, *120*, 6694–6703. [[CrossRef](#)]
39. Yamamoto, T.; Momida, H.; Hamada, T.; Uda, T.; Ohno, T. First-Principles Study of Dielectric Properties of Cerium Oxide. *Thin Solid Film.* **2005**, *486*, 136–140. [[CrossRef](#)]
40. Gurevich, V.L.; Tagantsev, A.K. Intrinsic Dielectric Loss in Crystals. *Adv. Phys.* **1991**, *40*, 719–767. [[CrossRef](#)]
41. Pei, J.; Yin, L.; Zhong, S.; Dang, Z. Suppressing the Loss of Polymer-Based Dielectrics for High Power Energy Storage. *Adv. Mater.* **2022**, *35*, 2203623. [[CrossRef](#)]
42. Fan, B.; Liu, F.; Yang, G.; Li, H.; Zhang, G.; Jiang, S.; Wang, Q. Dielectric Materials for High-temperature Capacitors. *IET Nanodielectrics* **2018**, *1*, 32–40. [[CrossRef](#)]
43. Selmi, M.; Smida, A.; Kossi, S.E. Effect of Polaron Formation in Conduction and Dielectric Behavior in La<sub>0.7</sub>Sr<sub>0.25</sub>KMnO<sub>3</sub> Oxide. *J. Mater. Sci. Mater. Electron.* **2021**, *32*, 6014–6027. [[CrossRef](#)]
44. Li, C.; Chen, G.; Qiu, X.; Lou, Q.; Gao, X. A Direct Proof for Maxwell–Wagner Effect of Heterogeneous Interface. *AIP Adv.* **2021**, *11*, 065227. [[CrossRef](#)]
45. Mironovich, A.Y.; Kostishin, V.G.; Shakirzyanov, R.I.; Mukabenov, A.A.; Melnikov, S.A.; Ril, A.I.; Al-Khafaji, H.I. Effect of the Fe/Ba and Fe/Sr Ratios on the Phase Composition, Dielectric Properties and Magnetic Characteristics of M-Type Hexaferrites Prepared by the Hydrothermal Method. *J. Solid State Chem.* **2022**, *316*, 123625. [[CrossRef](#)]
46. Hannay, J.H. The Clausius-Mossotti Equation: An Alternative Derivation. *Eur. J. Phys.* **1983**, *4*, 141–143. [[CrossRef](#)]
47. Thompson, D.P.; Dickins, A.M.; Thorp, J.S. The Dielectric Properties of Zirconia. *J. Mater. Sci.* **1992**, *27*, 2267–2271. [[CrossRef](#)]
48. Tang, Q.; Gong, J. Effect of Porosity on the Microhardness Testing of Brittle Ceramics: A Case Study on the System of NiO–ZrO<sub>2</sub>. *Ceram. Int.* **2013**, *39*, 8751–8759. [[CrossRef](#)]
49. Shakirzyanov, R.I.; Volodina, N.O.; Kadyrzhyanov, K.K.; Kozlovskiy, A.L.; Shlimas, D.I.; Baimbetova, G.A.; Borgekov, D.B.; Zdorovets, M.V. Study of the Aid Effect of CuO–TiO<sub>2</sub>–Nb<sub>2</sub>O<sub>5</sub> on the Dielectric and Structural Properties of Alumina Ceramics. *Materials* **2023**, *16*, 5018. [[CrossRef](#)]

50. Rejab, N.A.; Azhar, A.Z.A.; Ratnam, M.M.; Ahmad, Z.A. The Relationship between Microstructure and Fracture Toughness of Zirconia Toughened Alumina (ZTA) Added with MgO and CeO<sub>2</sub>. *Int. J. Refract. Met. Hard Mater.* **2013**, *41*, 522–530. [[CrossRef](#)]
51. Dudek, M. Ceramic Oxide Electrolytes Based on CeO<sub>2</sub>—Preparation, Properties and Possibility of Application to Electrochemical Devices. *J. Eur. Ceram. Soc.* **2008**, *28*, 965–971. [[CrossRef](#)]

**Disclaimer/Publisher's Note:** The statements, opinions and data contained in all publications are solely those of the individual author(s) and contributor(s) and not of MDPI and/or the editor(s). MDPI and/or the editor(s) disclaim responsibility for any injury to people or property resulting from any ideas, methods, instructions or products referred to in the content.